High-κ Dielectric on ReS$_2$: In-Situ Thermal Versus Plasma-Enhanced Atomic Layer Deposition of Al$_2$O$_3$

Ava Khosravi [1] ◉, **Rafik Addou** [1,2] ◉, **Massimo Catalano** [1,3], **Jiyoung Kim** [1] and **Robert M. Wallace** [1,*] ◉

[1] Department of Materials Science and Engineering, The University of Texas at Dallas, Richardson, TX 75080, USA; axk149530@utdallas.edu (A.K.); rafik.addou@oregonstate.edu (R.A.); mxc160230@utdallas.edu (M.C.); jiyoung.kim@utdallas.edu (J.K.)

[2] School of Chemical, Biological, and Environmental Engineering, Oregon State University, Corvallis, OR 93771, USA

[3] Institute for Microelectronics and Microsystems, National Council for Research (IMM-CNR), Via Monteroni, ed. A3, 73100 Lecce, Italy

[*] Correspondence: rmwallace@utdallas.edu; Tel.: +1-972-883-6638

Abstract: We report an excellent growth behavior of a high-κ dielectric on ReS$_2$, a two-dimensional (2D) transition metal dichalcogenide (TMD). The atomic layer deposition (ALD) of an Al$_2$O$_3$ thin film on the UV-Ozone pretreated surface of ReS$_2$ yields a pinhole free and conformal growth. In-situ half-cycle X-ray photoelectron spectroscopy (XPS) was used to monitor the interfacial chemistry and ex-situ atomic force microscopy (AFM) was used to evaluate the surface morphology. A significant enhancement in the uniformity of the Al$_2$O$_3$ thin film was deposited via plasma-enhanced atomic layer deposition (PEALD), while pinhole free Al$_2$O$_3$ was achieved using a UV-Ozone pretreatment. The ReS$_2$ substrate stays intact during all different experiments and processes without any formation of the Re oxide. This work demonstrates that a combination of the ALD process and the formation of weak S–O bonds presents an effective route for a uniform and conformal high-κ dielectric for advanced devices based on 2D materials.

Keywords: rhenium sulfide; atomic layer deposition; plasma-enhanced atomic layer deposition; X-ray photoelectron spectroscopy

1. Introduction

Transition metal dichalcogenides (TMDs) have emerged as strong candidates to be implemented as the semiconductor channel in Field Effect Transistor (FET) applications [1,2]. Their remarkable properties, such as sizable electronic bandgaps and the capability to scale down to sub-nanometer thickness, make semiconducting TMDs ideal candidates for applications in nanoelectronics [3]. Most semiconducting TMDs show significant changes in electronic properties from the bulk to the monolayer form, such as an indirect to direct band gap crossover [4]. Such properties provide opportunities to engineer material heterostructures to fit specific device requirements.

The reports on ReS$_2$ are relatively limited compared to other TMD materials. ReS$_2$ crystallizes in a distorted 1T phase, unlike most commonly studied TMDs, and this crystal structure causes unusual electronic and vibrational decoupling. Interestingly, the band gap type of ReS$_2$ in monolayer and bulk form remains uncertain. ReS$_2$ has been reported to have a direct bandgap, regardless of its thickness [5]. The ReS$_2$ direct bandgap is reported to be 1.35 eV in bulk and 1.42 eV in its monolayer form [6,7]. Recent computational and experimental studies address controversies on the band gap of ReS$_2$ [8–11]. Unlike early literature reports, such calculations revealed a layer dependence of the valence band

maximum (VBM) position in ReS_2 and indirect band gap character for bulk ReS_2 [12–14]. Recently, ReS_2-based FET devices have attracted interest [15–22], with a room temperature I_{on}/I_{off} ratio on the order of ~10^5 using few-layer ReS_2 flakes and Al_2O_3 as the high-κ top-gate dielectric [15]. In another report, top-gate FETs based on few-layer ReS_2 nanosheets encapsulated in an Al_2O_3 dielectric showed $I_{on}/I_{off} > 10^6$ [16]. Also, a high-performance ReS_2-based tunneling FET was reported to be exploiting an O_2 plasma treatment to accurately control the thickness of ReS_2 [18]. Such encouraging results suggest that ReS_2 could be a very promising candidate for future nanoelectronics.

When integrating TMDs into nanoelectronic devices, an optimized dielectric–semiconductor interface is crucial for TMD-based devices to reach commercial viability [23]. Previous reports demonstrate reduced Coulombic scattering and improved electron field-effect mobility in the TMD channel when interfacing with a high-κ dielectric [24]. Additionally, a conformal, pinhole-free dielectric layer inhibits the leakage current in a TMD-based device. However, the deposition of high-quality high-κ dielectrics onto the surface of TMD semiconductors has been a challenge due to the relative dearth of dangling bonds. The lower dangling bond density on the TMD surface causes the direct atomic layer deposition (ALD) of high-κ dielectrics to form islands instead of a continuous film [25]. The deposition of various dielectrics on 2D materials such as graphene, black phosphorus, MoS_2, and WSe_2 has been extensively studied [25–31]; however, a detailed interface investigation of a high-κ dielectric on ReS_2 and $ReSe_2$ remains of interest. Although a high-κ dielectric has been used for ReS_2 based devices [15,16,19], the ReS_2 interface chemistry with Al_2O_3 has not been reported. In this work, thermal ALD and PEALD (plasma-enhanced atomic layer deposition) are compared in order to study the high-κ dielectric interfacial chemistry. In-situ half-cycle X-ray photoelectron spectroscopy and ex-situ atomic force microscopy (AFM) and Raman have been used to explore this interface.

2. Materials and Methods

Bulk ReS_2 crystals purchased from HQ Graphene (Groningen, The Netherlands) were used to prepare clean surfaces by mechanical exfoliation using Scotch$^{(R)}$ Magic^{TM} tape (3M, Maplewood, MN, USA). Samples were loaded into an ultra-high vacuum (UHV) system, with 5 min of air exposure for an ALD/PEALD of Al_2O_3 and corresponding in-situ X-ray photoelectron spectroscopy (XPS, Sienta Omicron GmbH, Taunusstein, Germany) analysis. The UHV apparatus (base pressure ~10^{-10} mbar) and XPS employed in this work are described in detail elsewhere [32]. Samples were annealed at 250 °C in a chamber (base pressure ~10^{-9} mbar) under UHV for 1 h prior to the ALD processes, to desorb the adventitious carbon and oxygen from the sample surface (Figure S1a,b). After annealing, the surface chemistry of the sample did not change (Figure S1c,d). The UHV system was connected to the PEALD chamber (Picosun PR200, Espoo, Finland) through an intermediate chamber. A trimethylaluminum (TMA) and H_2O (pulse time of 0.1 s and a 4.0 s Ar purge) were used for the thermal ALD process. During the PEALD process, TMA with a 0.1 s pulse time and a 4.0 s Ar purge, and a remote O_2 plasma with a 3.0 s pulse and 4.0 s Ar purge were used as precursors. A Litmas RF-plasma source (RF power 2000 W) with an O_2 gas flow of 120 sccm generated the remote O_2 plasma. The deposition chamber (base pressure of 3 mbar) was held at 200 °C throughout all deposition processes of this work. The nucleation and the growth of Al_2O_3 by ALD and PEALD was studied by means of an in-situ half-cycle process. The XPS scans were measured following each successive half cycle, up to five full cycles and following 10, 40, and 80 full ALD/PEALD cycles (Figure S2). Each XPS spectra was recorded using a monochromatic Al Kα x-ray source with an Omicron EA125 hemispherical analyzer (Sienta Omicron GmbH, Taunusstein, Germany, pass energy of a 15 eV and a resolution of ±0.05 eV). AAnalyzer Version 1.36 software was used to deconvolute the XPS data [33]. An ex-situ atomic force microscope (AFM, Veeco Model 3100 Dimension V, Veeco, Plainview, NY, USA), operating in the tapping mode under ambient conditions, was also used to characterize the surface morphology after 80 full cycles of each process, and WSxM was used to analyze the AFM images [34]. An ex-situ Raman measurement was also acquired by a 532 nm wavelength laser with 0.22 mW power and ~500 nm spot size. The atomic Scanning Transmission Electron Microscope High-Angle Annular Dark-Field (STEM

HAADF) images were obtained using a JEOL ARM200F microscope (JEOL, Tokyo, Japan) equipped with a spherical aberration (Cs) corrector (CEOS GmbH, Heidelberg, Germany) and operated at 200 kV. The corrector was carefully tuned by the Zemlin tableau method with Cs$\frac{1}{4}$ 0.5 lm, and the resolution was demonstrated to be around 0.1 nm.

3. Results and Discussion

3.1. Surface Analysis of the Exfoliated ReS$_2$ Surface

Figure 1a,b show the S 2p and Re 4f core level spectra, measured on an as-exfoliated ReS$_2$ surface. It is important to note that we found two distinct states (red and blue spectra) in the S 2p core level in all samples studied in this work. These states are separated by 0.6 eV, and the ratio between their areas is 0.7. The binding energy of the S 2$p_{3/2}$ core level of elemental sulfur (S^0) is reported to be ~164.0 eV, which was not detected here [35]. Since there is no chemical state detected in the O 1s core level at ~530 eV (Figure S1b), the additional sulfur chemical state cannot be assigned to the formation of a S–O bond [26]. The same S 2p core level spectrum line shape has been shown in previous XPS reports of ReS$_2$ [36–41]; however, the S 2p doublets were not examined carefully, and a second state was not detected. Other reports on distorted 1T-ReS$_2$ show a similar binding energy separation (0.6 eV) in the S 2p core level [39,40]. An additional state in the Re 4f core level was detected at a 0.6 eV lower binding energy than the most intense peak for all samples used in this study (red spectra, Figure 1b). The metallic Re (Re^0) state appears at a 1.1 eV lower binding energy from the Re^{4+} chemical state however, the binding energy separation between the two Re 4f doublets detected here is smaller (red and blue curves, Figure 1b) [40]. The additional state is not associated with the Re–O chemical state, as Re–O should be detected at a higher binding energy [42]. This extra feature at the lower binding energy in the Re 4f core level could be the result of surface roughness or defects [43]. The separation between the S 2$p_{5/2}$ and Re 4$f_{7/2}$ core levels for the distorted 1T-ReS$_2$ phase (blue spectra, Figure 1) was 120.4 eV, in agreement with the previous report [44]. Interestingly, the S:Re ratio is 2:1 when considering the integrated area of both states (both red and blue spectra) in the S 2p and Re 4f core levels, while the S:Re ratio is only 1:1 when considering only the high binding energy state in the S 2p core level (blue spectra). The extra features at both S 2p and Re 4f were detected at different spots on the same sample, as well as on the same sample following a second exfoliation.

A flake from an exfoliated ReS$_2$ sample was imaged using STEM, as shown by the plan view in Figure 1c. ReS$_2$ has triclinic symmetry in the crystal structure, wherein Re atoms in the layer form a zigzag Re–Re chain [17,20,45]. Figure 1c provides a view of the crystalline structure of the ReS$_2$, and shows that the four Re atoms are arranged in a diamond-like shape and form atomic chains. The atomic structure confirms the distorted 1T phase, as suggested by previous investigations [20,36,45]. The TEM data show the presence of only one dominant distorted 1T phase in the ReS$_2$ flakes. To further study the crystal structure of ReS$_2$, Raman spectroscopy was performed on as-exfoliated bulk ReS$_2$, showing conclusive evidence of having a distorted 1T structure. Because of the low symmetry of the distorted 1T phase, 18 Raman peaks were found in the range of 100–500 cm^{-1} in bulk ReS$_2$, consistent with previous studies [46,47]. The primary Raman active modes at 150.2 cm^{-1} and 211.0 cm^{-1}, associated with Eg-like and Ag-like modes, are presented in Figure 1d [48,49].
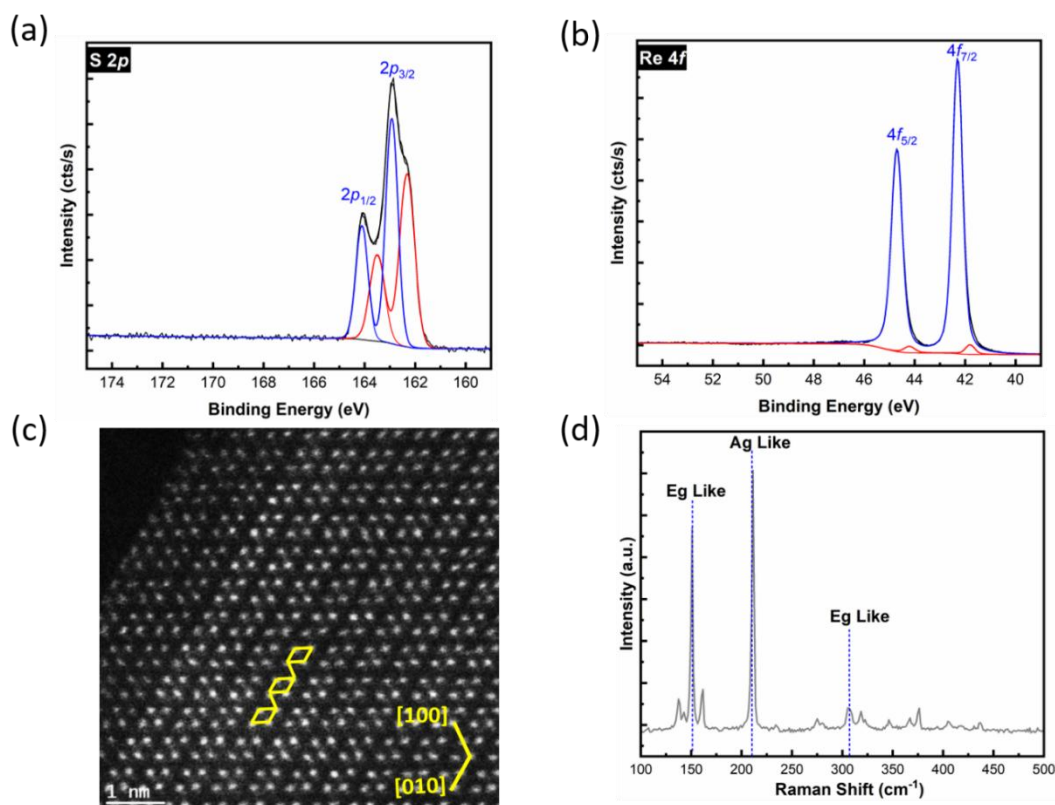
Figure 1. (**a**) S 2*p* and (**b**) Re 4*f* X-ray photoelectron spectroscopy (XPS) core level spectra obtained on a freshly exfoliated ReS$_2$ surface. The additional component in the lower binding energy is shown in red for both spectra. (**c**) High-angle annular dark field (HAADF) presents only Re atoms and (**d**) Raman spectrum of exfoliated ReS$_2$.

Thermal ALD of Al$_2$O$_3$ on ReS$_2$

The evolution of the Re 4*f* and S 2*p* core levels throughout the thermal ALD of Al$_2$O$_3$ is shown in Figure 2a. The Re 4*f* and S 2*p* core level spectra were obtained from the ReS$_2$ surface after in-situ annealing, after the first successive half-cycle of TMA and H$_2$O, after the fifth half-cycle of TMA and H$_2$O, and following 10, 40, and 80 full cycles of Al$_2$O$_3$. Only the XPS of the first and fifth half-cycle exposures are shown, as no significant changes occurred in the surface chemistry in between these measurements. Figure 2a indicates that the ReS$_2$ sample is free of any additional chemical states in the Re 4*f* or S 2*p* core levels throughout the thermal ALD process, other than the state discussed above (Figure 1a,b), and rhenium oxide or sulfur oxide compounds (Re–O, Re–O–S, or S–O bonds) are below the XPS detection limit. The acquisition of XPS spectra for the Re 4*f* and S 2*p* core levels were extended on the higher binding energy side up to 55 eV and 175 eV (Figure 1a,b), respectively, to ensure that there were no additional chemical states at the Re 4*f* and S 2*p* core level spectra. Depositing Al$_2$O$_3$ on ReS$_2$ decreases the intensities of the Re 4*f* and S 2*p* core levels (Figure 2a) due to XPS signal attenuation. However, the Re 4*f* and S 2*p* core levels are still clearly detectable even after 80 full cycles of thermal ALD due to the clustering of the Al$_2$O$_3$ film, as suggested by the ex-situ AFM topographic image in Figure 2b. At the initial stage, the slow growth rate indicates that thermal ALD of Al$_2$O$_3$ on the untreated ReS$_2$ surface requires 10 thermal ALD cycles to nucleate, displaying the *substrate-inhibited* growth.
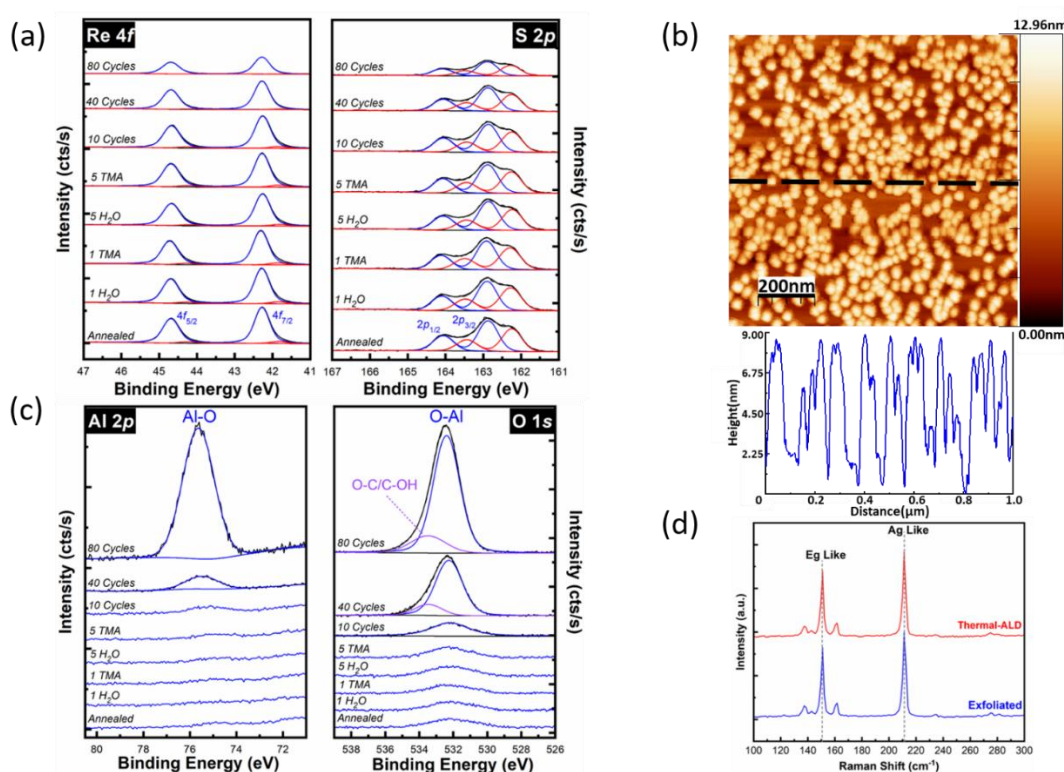
Figure 2. Thermal atomic layer deposition (ALD) of Al_2O_3 on ReS_2. (**a**) The evolution of Re 4*f* and S 2*p* core level spectra, (**b**) Ex-situ AFM image and line profile recorded following 80 cycles ALD of Al_2O_3, (**c**) Al 2p and O 1s core level spectra up to 80 cycles of Al_2O_3, and (**d**) Raman spectra comparison between exfoliated ReS_2 and following 80 cycles of ALD of Al_2O_3.

Figure 2b shows a topographic image obtained by AFM of Al_2O_3 on ReS_2 following 80 full cycles employing the thermal ALD process. After the thermal ALD on ReS_2, an islanding growth is observed because of the relative dearth of dangling bonds on 2D TMD surfaces [25,26]. The AFM line profile shows that the height of these Al_2O_3 islands is ~8 nm, with a root mean square (RMS) surface roughness of 2.7 nm.

The corresponding Al 2p and O 1s core level spectra measured during the thermal ALD process are shown in Figure 2c. Aluminum remains near the XPS detection limit in the Al 2p core level following Al_2O_3 deposition up to 10 thermal ALD cycles. After 10 full cycles of Al_2O_3, the peak at 75.4 eV caused by the formation of Al–O bonds starts to increase, with an increasing number of ALD cycles. The analysis of this peak in the Al 2p core level after 40 and 80 full cycles reveals the formation of an Al_2O_3 film on ReS_2. The line shape of the background intensity at the Al 2p core level increases at lower binding energies due to the presence of a Re 4*f* loss feature at 68 eV (Figure S3). After annealing, a small amount of oxygen (7.0 atomic%) was still detectable on the surface of the ReS_2 sample (Figure 2c). The O 1s core level shown in Figure 2c after 40 and 80 full ALD cycles is deconvoluted into two peaks. The peak at 532.3 eV is associated with the Al−O chemical state and the peak at the higher binding energy (533.5 eV) is attributed to intermediate species, such as carbonyl and formate [28,50].

ReS_2 samples characterized via ex-situ Raman spectroscopy following thermal ALD are consistent with the Raman spectra recorded on an as-exfoliated ReS_2 surface [46,47]. Amorphous Al_2O_3 on the surface does not affect the Raman spectra of the substrate, and therefore structural changes through different processes of this work should be observable. Figure 2d shows the Raman spectra from as-exfoliated ReS_2 and after 80 cycles thermal ALD of Al_2O_3. Two prominent Raman peaks at 150.2 cm^{-1} and 211.0 cm^{-1} are assigned to E_g-like and A_g-like vibrational modes, respectively [51].

In TMDs, Raman active modes have been reported to shift with changes in strain [52], temperature [53], and doping [54]. Figure 2d confirms that ReS_2 remains unaffected following the annealing and the ALD process.

3.2. Plasma-Enhanced ALD of Al_2O_3 on ReS_2

PEALD has been reported to achieve conformal high-κ dielectrics on the TMD surface without utilizing any surface pretreatment [55]. Based on this study, PEALD is used to improve the coverage of deposited Al_2O_3 on ReS_2. More importantly, this work studies the interfacial chemistry changes during the PEALD process on ReS_2. Similar to the thermal ALD process, an in-situ half-cycle PEALD study was performed to monitor the chemistry of the Al_2O_3/ReS_2 interface. Figure 3a shows the Re 4*f* and S 2*p* core level spectra obtained from the annealed surface, after the first half-cycle of O_2 plasma and TMA, after the fifth half-cycles of O_2 plasma and TMA, and following 10, 40, and 80 full cycles of Al_2O_3. No additional chemical states were detected in the Re 4*f* or S 2*p* core levels on the surface of the annealed ReS_2 sample. After the first pulse of remote O_2 plasma, an additional chemical state in the corresponding S 2*p* core level was detected at 164.8 eV (Figure 3a, green peaks), which was concurrent with the appearance of an additional chemical state at a lower binding energy (530.5 eV) in the corresponding O 1s core level in Figure 3c.
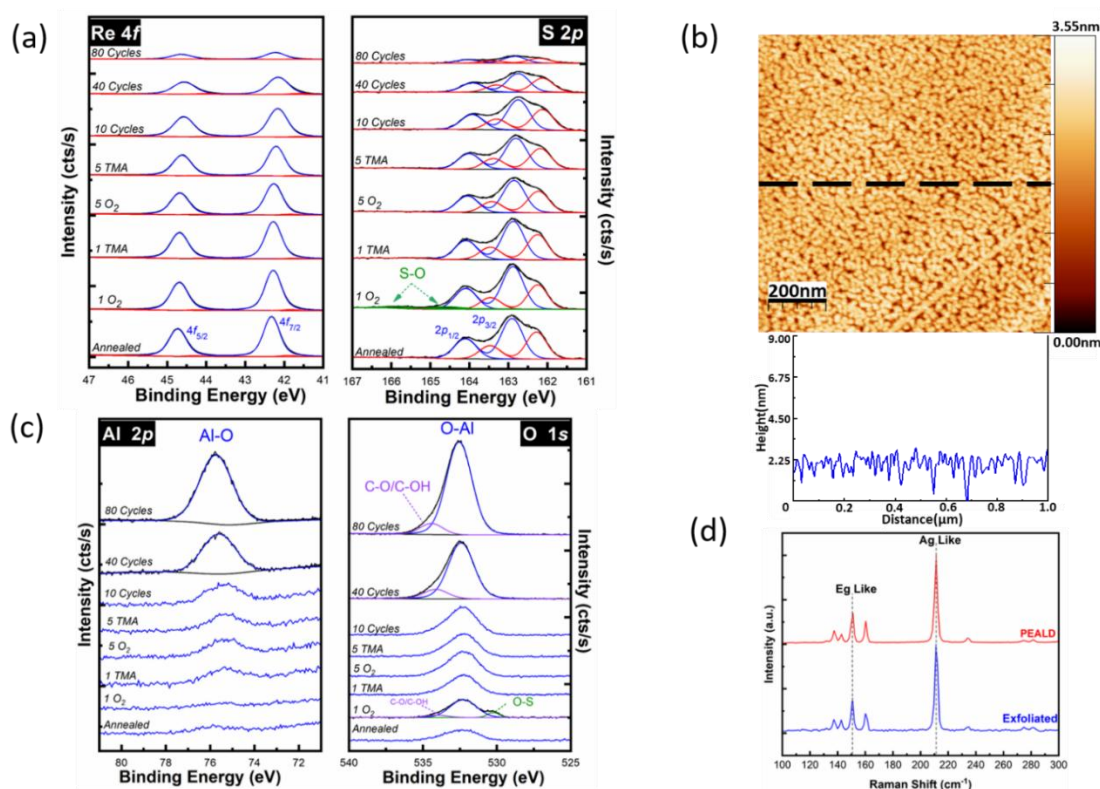

Figure 3. Plasma-enhanced atomic layer deposition (PEALD) of Al_2O_3 on ReS_2. (**a**) The evolution of (**a**) Re 4*f* and S 2*p* core level spectra, (**b**) Ex-situ AFM image and line profile recorded following 80 cycles PEALD of Al_2O_3, (**c**) Al 2p and O 1s core level spectra up to 80 cycles of Al_2O_3, and (**d**) Raman spectra recorded on exfoliated ReS_2 and after 80 cycles of PEALD of Al_2O_3.

This additional chemical state corresponds to the S–O bonds created by the remote O_2 plasma pulse. We estimated an oxidation of ~4.0% of S atoms on the surface after the first O_2 plasma pulse. The S–O chemical bonds on the ReS_2 surface act as nucleation sites, making the surface more reactive with the precursors. Through ligand exchange reactions, the S–O bonds are cleaned up by the successive TMA pulse and fall below the XPS detection limit [56]. During the rest of the PEALD

process, the S–O chemical state remains below the XPS detection limit, and the ReS$_2$ surface is free of any additional chemical states in the Re 4f or S 2p core levels, consistent with an abrupt interface. The first noticeable observation is that depositing Al$_2$O$_3$ on ReS$_2$ using PEALD significantly decreases the intensities of the Re 4f and S 2p core levels from the substrate after 80 full cycles of PEALD, in comparison to thermal ALD (Figure 2a), which suggests better Al$_2$O$_3$ coverage on ReS$_2$. This is consistent with the corresponding AFM topographic image in Figure 3b. The difference in thermal ALD and PEALD deposition after 80 cycles could be explained with the creation of S–O bonds as a reactive nucleation center in the PEALD method. Figure 3b shows the surface morphology of the sample after 80 PEALD cycles of Al$_2$O$_3$. The PEALD process results in a better coverage of the Al$_2$O$_3$ film with an RMS surface roughness of 0.49 nm compared to the thermal ALD process. The XPS-estimated Al$_2$O$_3$ thickness was 2.3 nm, which was calculated based on the substrate signal attenuation of the S 2p core level integrated intensity (Supplementary Materials, Section 3). The thickness calculated by XPS is underestimated due to the detection of the substrate signal through pinholes in the oxide film.

Figure 3c shows the evolution of the Al 2p and O 1s core level spectra of the PEALD process. Unlike the thermal ALD process, a small Al 2p peak is detected at 75.4 eV after the first TMA pulse, suggesting that, with the PEALD process, Al is deposited on the ReS$_2$ surface without any inhibition time. The peak associated with the Al–O chemical state in Al 2p and O 1s core level spectra keeps increasing throughout the PEALD process. Similar to the thermal ALD process, the O 1s core level is deconvoluted into two main components of an Al–O chemical state at a low binding energy and an intermediate species chemical state at a higher binding energy. The ReS$_2$ structure was monitored via ex-situ Raman spectroscopy before and after the PEALD (Figure 3d). The two prominent Raman peaks—E$_g$-like at 150.2 cm^{-1} and A$_g$-like at 211.0 cm^{-1}—do not show any noticeable changes, confirming the stability of the ReS$_2$ structure under the remote O$_2$ plasma exposure of PEALD process.

The PEALD method results in a better coverage and lower root mean square (RMS) surface roughness due to a better nucleation and thus a thicker Al$_2$O$_3$ layer, as suggested by the associated XPS and AFM measurements. The PEALD of Al$_2$O$_3$ is greatly improved the low coverage and clustering behavior associated with the thermal ALD of Al$_2$O$_3$ on ReS$_2$, however, pinholes with ~2 nm depth are observed, based on AFM measurements. Despite the improvement in Al$_2$O$_3$ coverage achieved with the PEALD process via the creation of S–O bonds, neither thermal ALD or PEALD yield conformal, pinhole-free Al$_2$O$_3$ on ReS$_2$.

3.3. Al$_2$O$_3$ on A UV-Ozone Exposed ReS$_2$ Surface

To grow a uniform dielectric layer on TMDs, a number of surface functionalization methods were proposed, such as UV-Ozone pre-treatment [26,57], oxygen plasma pre-treatment [58], the use of ozone as the oxidant precursor during the ALD of Al$_2$O$_3$ [28], and metal-oxide seed layers [59]. Based on the PEALD results of this work on ReS$_2$ and the previous study on MoS$_2$ [26,60], the formation of S–O in sulfur-based TMD materials seems to be a promising route for surface functionalization. To further improve the surface coverage of Al$_2$O$_3$ on the ReS$_2$, the sample is exposed to UV-Ozone as a surface pretreatment to form S–O bonds, and then subjected to the standard thermal ALD process. An in-situ study of the UV-Ozone exposure of ReS$_2$ was performed and chemical state changes were monitored by XPS. The UV photons from a low-pressure mercury lamp were used to produce ozone in a chamber (base pressure of ~10^{-9} mbar) which was filled with O$_2$ to a pressure of 900 mbar [61]. Then, the sample was transferred in-situ to the ALD chamber for Al$_2$O$_3$ deposition with TMA and H$_2$O. Figure 4a shows the Re 4f and S 2p core level spectra obtained from the annealed surface after 15 min UV-Ozone exposure, after the first successive half-cycle of H$_2$O and TMA, after the fifth half-cycle of H$_2$O and TMA, and following 10, 40, and 80 full cycles of Al$_2$O$_3$. After UV-Ozone exposure, an additional chemical state is detected in the S 2p core level at 164.8 eV (Figure 4a), which suggests the formation of S–O bonds [26]. The Re–O chemical state is below the XPS detection limit after the UV-Ozone exposure. We estimate ~12% of S atoms on the surface are oxidized after UV-Ozone treatment, but the S/Re ratio remains identical to the initial substrate. Following the first pulse of TMA, the S–O chemical

state falls below the XPS detection limit. Similar to the PEALD process, during the rest of the thermal ALD process the S–O chemical state stays under the XPS detection limit. After 80 cycles of TMA/H$_2$O deposition, sulfur is below the XPS detection limit due to the signal attenuation of the deposited Al$_2$O$_3$. In addition, the Re 4*f* core level intensity is significantly decreased, making it difficult to deconvolve. Significant attenuation of Re 4*f* and S 2*p* core levels suggest that Al$_2$O$_3$ is comparable to the XPS depth of detection (~5 nm). The topographical AFM image of the Al$_2$O$_3$ film following 80 full cycles of Al$_2$O$_3$ deposition through the thermal ALD on a UV-Ozone pretreated ReS$_2$ surface is shown in Figure 4b. The AFM image shows a conformal and pinhole free film with a very low RMS roughness of 0.11 nm, consistent with XPS analysis.
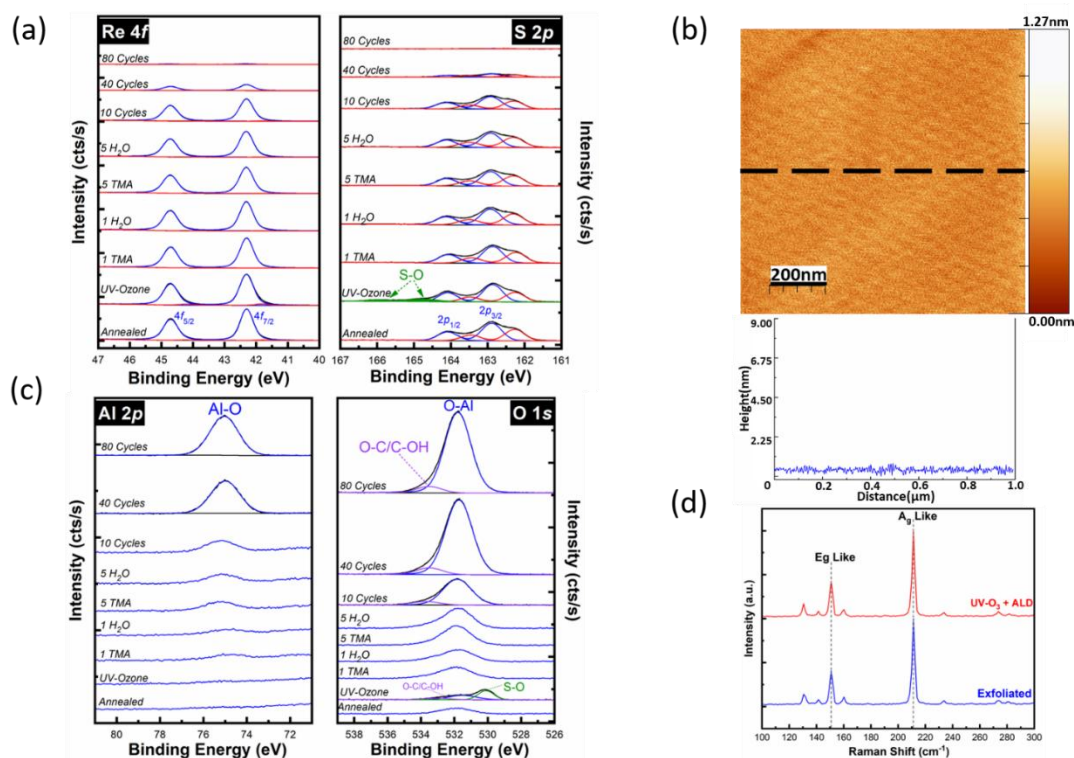
Figure 4. Deposition of Al$_2$O$_3$ using thermal ALD on functionalized ReS$_2$ surface by UV-Ozone exposure. (**a**) The evolution of Re 4*f* and S 2*p* core level spectra, (**b**) Ex-situ AFM image and line profile recorded following 80 cycles PEALD of Al$_2$O$_3$, (**c**) Al 2p and O 1s core level spectra up to 80 cycles of Al$_2$O$_3$, and (**d**) Raman spectra from exfoliated ReS$_2$ and after 80 cycles of Al$_2$O$_3$ on UV-Ozone treated ReS$_2$.

Figure 4c shows the evolution of the Al 2*p* and O 1*s* core level spectra. In the Al 2*p* core level, a peak is discernable at ~75 eV after the first TMA exposure, however, it is in the order of the XPS detection limit until the fifth TMA pulse. The O 1*s* core level again indicates the presence of two main components: an Al–O chemical state at low binding energy and an intermediate species chemical state at high binding energy. Utilizing the UV-Ozone pretreatment as a surface functionalization to deposit a thin Al$_2$O$_3$ film by thermal ALD produces the highest quality (conformal, pinhole-free) film on ReS$_2$ in this work. The ex-situ Raman spectra of the ReS$_2$ sample before and after being exposed to UV-Ozone at room temperature for 15 min and following 80 cycles of thermal ALD are shown in Figure 4d. Similar to the other processes, the Raman spectra did not show any changes after UV-Ozone exposure, demonstrating that the ReS$_2$ structure stays intact.

Although both PEALD and the UV-Ozone pretreatment create S–O bonding on the surface, which serves as nucleation centers for subsequent ALD, the difference in the nucleation and Al$_2$O$_3$ growth behavior between the two methods is clear from AFM images. One important difference is that

a higher S–O concentration was found for the UV-Ozone exposure in comparison to after the first O_2 pulse in PEALD. This higher concentration of S–O bonds on the ReS_2 surface helped with the pinhole issue of PEALD. Moreover, the concentration of the organic surface contamination after the UV-Ozone process is significantly less than after the PEALD process, as shown in the C 1s and O 1s XPS core level spectra (Figure S4). It is important to note that the prolonged X-ray exposure and UHV conditions occurred during the half-cycle XPS study do not change the surface chemistry of bulk ReS_2 sample as indicated in Figure S5.

4. Conclusions

In summary, to achieve pinhole free and conformal high-κ dielectric on ReS_2 substrate, we investigated different approaches for the growth of Al_2O_3. In-situ half-cycle XPS and ex-situ AFM were exploited to study the surface/interface chemistry and morphology of ReS_2 after thermal ALD, PEALD, and UV-Ozone surface functionalization prior to ALD. Half-cycle XPS revealed that the ReS_2 initial surface changes after the few first pulses of each process. The growth of Al_2O_3 by traditional ALD follows a substrate inhibited growth behavior, where an incubation period is required, followed by an islanding growth mode. However, the PEALD process enhances the growth of deposited Al_2O_3 by the creation of S–O bonds, but pinholes are still detectable even with lower RMS in comparison to the ALD growth. AFM images in conjunction with XPS data show that the UV-Ozone treatment is a practical route for the functionalization of ReS_2 prior to ALD, to get a conformal coverage of Al_2O_3. Raman Spectroscopy and the XPS S/Re ratio confirms the structural stability of ReS_2 under O_2 plasma and UV-Ozone treatment.

References

1. Amani, M.; Chin, M.L.; Birdwell, A.G.; O'Regan, T.P.; Najmaei, S.; Liu, Z.; Ajayan, P.M.; Lou, J.; Dubey, M. Electrical performance of monolayer MoS_2 field-effect transistors prepared by chemical vapor deposition. *Appl. Phys. Lett.* **2013**, *102*, 193107. [CrossRef]

2. Nourbakhsh, A.; Zubair, A.; Sajjad, R.N.; Tavakkoli KG, A.; Chen, W.; Fang, S.; Ling, X.; Kong, J.; Dresselhaus, M.S.; Kaxiras, E. MoS_2 field-effect transistor with sub-10 nm channel length. *Nano Lett.* **2016**, *16*, 7798–7806. [CrossRef] [PubMed]

3. Akinwande, D.; Petrone, N.; Hone, J. Two-dimensional flexible nanoelectronics. *Nat. Commun.* **2014**, *5*, 5678. [CrossRef]

4. Wang, Q.H.; Kalantar-Zadeh, K.; Kis, A.; Coleman, J.N.; Strano, M.S. Electronics and optoelectronics of two-dimensional transition metal dichalcogenides. *Nat. Nanotechnol.* **2012**, *7*, 699. [CrossRef] [PubMed]

5. Tongay, S.; Sahin, H.; Ko, C.; Luce, A.; Fan, W.; Liu, K.; Zhou, J.; Huang, Y.-S.; Ho, C.-H.; Yan, J. Monolayer behaviour in bulk ReS_2 due to electronic and vibrational decoupling. *Nat. Commun.* **2014**, *5*, 3252. [CrossRef] [PubMed]

6. Horzum, S.; Çakır, D.; Suh, J.; Tongay, S.; Huang, Y.-S.; Ho, C.-H.; Wu, J.; Sahin, H.; Peeters, F. Formation and stability of point defects in monolayer rhenium disulfide. *Phys. Rev. B* **2014**, *89*, 155433. [CrossRef]

7. Yu, Z.G.; Cai, Y.; Zhang, Y.-W. Robust Direct Bandgap Characteristics of One-and Two-Dimensional ReS_2. *Sci. Rep.* **2015**, *5*, 13783. [CrossRef] [PubMed]

8. Zong, J.-Q.; Zhang, S.-F.; Ji, W.-X.; Zhang, C.-W.; Li, P.; Wang, P.-J. Electric structure and optical properties of ReS$_2$ nanomaterials. *Superlattice Microst.* **2018**, *122*, 262–267. [CrossRef]

9. Echeverry, J.; Gerber, I. Theoretical investigations of the anisotropic optical properties of distorted 1T ReS$_2$ and ReSe$_2$ monolayers, bilayers, and in the bulk limit. *Phys. Rev. B* **2018**, *97*, 075123. [CrossRef]

10. Gutiérrez-Lezama, I.; Reddy, B.A.; Ubrig, N.; Morpurgo, A.F. Electroluminescence from indirect band gap semiconductor ReS$_2$. *2D Mater.* **2016**, *3*, 045016. [CrossRef]

11. Webb, J.L.; Hart, L.S.; Wolverson, D.; Chen, C.; Avila, J.; Asensio, M.C. Electronic band structure of ReS$_2$ by high-resolution angle-resolved photoemission spectroscopy. *Phys. Rev. B* **2017**, *96*, 115205. [CrossRef]

12. Gehlmann, M.; Aguilera, I.; Bihlmayer, G.; Nemsák, S.; Nagler, P.; Gospodaric, P.; Zamborlini, G.; Eschbach, M.; Feyer, V.; Kronast, F. Direct observation of the band gap transition in atomically thin ReS$_2$. *Nano Lett.* **2017**, *17*, 5187–5192. [CrossRef] [PubMed]

13. Gunasekera, S.M.; Wolverson, D.; Hart, L.S.; Mucha-Kruczynski, M. Electronic band structure of rhenium dichalcogenides. *J. Electron. Mater.* **2018**, *47*, 1–7. [CrossRef]

14. Hart, L.S.; Webb, J.L.; Dale, S.; Bending, S.J.; Mucha-Kruczynski, M.; Wolverson, D.; Chen, C.; Avila, J.; Asensio, M.C. Electronic bandstructure and van der Waals coupling of ReSe$_2$ revealed by high-resolution angle-resolved photoemission spectroscopy. *Sci. Rep.* **2017**, *7*, 5145. [CrossRef] [PubMed]

15. Corbet, C.M.; McClellan, C.; Rai, A.; Sonde, S.S.; Tutuc, E.; Banerjee, S.K. Field effect transistors with current saturation and voltage gain in ultrathin ReS$_2$. *ACS Nano* **2014**, *9*, 363–370. [CrossRef] [PubMed]

16. Zhang, E.; Jin, Y.; Yuan, X.; Wang, W.; Zhang, C.; Tang, L.; Liu, S.; Zhou, P.; Hu, W.; Xiu, F. ReS$_2$-Based Field-Effect Transistors and Photodetectors. *Adv. Funct. Mater.* **2015**, *25*, 4076–4082. [CrossRef]

17. He, X.; Liu, F.; Hu, P.; Fu, W.; Wang, X.; Zeng, Q.; Zhao, W.; Liu, Z. Chemical Vapor Deposition of High-Quality and Atomically Layered ReS$_2$. *Small* **2015**, *11*, 5423–5429. [CrossRef] [PubMed]

18. Shim, J.; Oh, A.; Kang, D.H.; Oh, S.; Jang, S.K.; Jeon, J.; Jeon, M.H.; Kim, M.; Choi, C.; Lee, J. High-Performance 2D Rhenium Disulfide (ReS$_2$) Transistors and Photodetectors by Oxygen Plasma Treatment. *Adv. Mater.* **2016**, *28*, 6985–6992. [CrossRef] [PubMed]

19. Liu, E.; Fu, Y.; Wang, Y.; Feng, Y.; Liu, H.; Wan, X.; Zhou, W.; Wang, B.; Shao, L.; Ho, C.-H. Integrated digital inverters based on two-dimensional anisotropic ReS$_2$ field-effect transistors. *Nat. Commun.* **2015**, *6*, 6991. [CrossRef] [PubMed]

20. Lin, Y.-C.; Komsa, H.-P.; Yeh, C.-H.; Bjorkman, T.; Liang, Z.-Y.; Ho, C.-H.; Huang, Y.-S.; Chiu, P.-W.; Krasheninnikov, A.V.; Suenaga, K. Single-layer ReS$_2$: Two-dimensional semiconductor with tunable in-plane anisotropy. *ACS Nano* **2015**, *9*, 11249–11257. [CrossRef]

21. Liao, W.; Wei, W.; Tong, Y.; Chim, W.K.; Zhu, C. Low-Frequency Noise in Layered ReS$_2$ Field Effect Transistors on HfO$_2$ and Its Application for pH Sensing. *ACS Appl. Mater. Interfaces* **2018**, *10*, 7248–7255. [CrossRef]

22. Park, J.Y.; Joe, H.-E.; Yoon, H.S.; Yoo, S.; Kim, T.; Kang, K.; Min, B.-K.; Jun, S.C. Contact effect of ReS$_2$/metal interface. *ACS Appl. Mater. Interfaces* **2017**, *9*, 26325–26332. [CrossRef] [PubMed]

23. Addou, R.; Wallace, R.M. Using Photoelectron Spectroscopy in the Integration of 2D Materials for Advanced Devices. *J. Electron. Spectrosc. Relat. Phenom.* **2019**, *231*, 94–103. [CrossRef]

24. Jena, D.; Konar, A. Enhancement of carrier mobility in semiconductor nanostructures by dielectric engineering. *Phys. Rev. Lett.* **2007**, *98*, 136805. [CrossRef] [PubMed]

25. McDonnell, S.; Brennan, B.; Azcatl, A.; Lu, N.; Dong, H.; Buie, C.; Kim, J.; Hinkle, C.L.; Kim, M.J.; Wallace, R.M. HfO$_2$ on MoS$_2$ by atomic layer deposition: Adsorption mechanisms and thickness scalability. *ACS Nano* **2013**, *7*, 10354–10361. [CrossRef]

26. Azcatl, A.; McDonnell, S.; KC, S.; Peng, X.; Dong, H.; Qin, X.; Addou, R.; Mordi, G.I.; Lu, N.; Kim, J. MoS$_2$ functionalization for ultra-thin atomic layer deposited dielectrics. *Appl. Phys. Lett.* **2014**, *104*, 111601. [CrossRef]

27. Azcatl, A.; Wang, Q.; Kim, M.J.; Wallace, R.M. Al$_2$O$_3$ on WSe$_2$ by ozone based atomic layer deposition: Nucleation and interface study. *APL Mater.* **2017**, *5*, 086108. [CrossRef]

28. Cheng, L.; Qin, X.; Lucero, A.T.; Azcatl, A.; Huang, J.; Wallace, R.M.; Cho, K.; Kim, J. Atomic layer deposition of a high-k dielectric on MoS$_2$ using trimethylaluminum and ozone. *ACS Appl. Mater. Interfaces* **2014**, *6*, 11834–11838. [CrossRef]

29. Zhu, H.; McDonnell, S.; Qin, X.; Azcatl, A.; Cheng, L.; Addou, R.; Kim, J.; Ye, P.D.; Wallace, R.M. Al$_2$O$_3$ on black phosphorus by atomic layer deposition: An in-situ interface study. *ACS Appl. Mater. Interfaces* **2015**, *7*, 13038–13043. [CrossRef]

30. Dahal, A.; Addou, R.; Azcatl, A.; Coy-Diaz, H.; Lu, N.; Peng, X.; de Dios, F.; Kim, J.; Kim, M.J.; Wallace, R.M. Seeding Atomic Layer Deposition of Alumina on Graphene with Yttria. *ACS Appl. Mater. Interfaces* **2015**, *7*, 2082–2087. [CrossRef]

31. Addou, R.; Dahal, A.; Batzill, M. Growth of a two-dimensional dielectric monolayer on quasi-freestanding graphene. *Nat. Nanotechnol.* **2013**, *8*, 41. [CrossRef] [PubMed]

32. Wallace, R.M. In-Situ Studies on 2D Materials. *ECS Trans.* **2014**, *64*, 109–116. [CrossRef]

33. Herrera-Gomez, A.; Hegedus, A.; Meissner, P. Chemical depth profile of ultrathin nitrided SiO_2 films. *Appl. Phys. Lett.* **2002**, *81*, 1014–1016. [CrossRef]

34. Horcas, I.; Fernández, R.; Gomez-Rodriguez, J.; Colchero, J.; Gómez-Herrero, J.; Baro, A. WSXM: A software for scanning probe microscopy and a tool for nanotechnology. *Rev. Sci. Instrum.* **2007**, *78*, 013705. [CrossRef] [PubMed]

35. Xie, L.; Wang, J.; Shi, C.; Huang, J.; Zhang, H.; Liu, Q.; Liu, Q.; Zeng, H. Probing surface interactions of electrochemically active galena mineral surface using atomic force microscopy. *J. Phys. Chem. C* **2016**, *120*, 22433–22442. [CrossRef]

36. Cui, F.; Wang, C.; Li, X.; Wang, G.; Liu, K.; Yang, Z.; Feng, Q.; Liang, X.; Zhang, Z.; Liu, S. Tellurium-Assisted Epitaxial Growth of Large-Area, Highly Crystalline ReS_2 Atomic Layers on Mica Substrate. *Adv. Mater.* **2016**, *28*, 5019–5024. [CrossRef] [PubMed]

37. Wang, L.; Sofer, Z.; Luxa, J.; Sedmidubský, D.; Ambrosi, A.; Pumera, M. Layered rhenium sulfide on free-standing three-dimensional electrodes is highly catalytic for the hydrogen evolution reaction: Experimental and theoretical study. *Electrochem. Commun.* **2016**, *63*, 39–43. [CrossRef]

38. Zhang, Q.; Tan, S.; Mendes, R.G.; Sun, Z.; Chen, Y.; Kong, X.; Xue, Y.; Rümmeli, M.H.; Wu, X.; Chen, S. Extremely Weak van der Waals Coupling in Vertical ReS_2 Nanowalls for High-Current-Density Lithium-Ion Batteries. *Adv. Mater.* **2016**, *28*, 2616–2623. [CrossRef]

39. Fujita, T.; Ito, Y.; Tan, Y.; Yamaguchi, H.; Hojo, D.; Hirata, A.; Voiry, D.; Chhowalla, M.; Chen, M. Chemically exfoliated ReS_2 nanosheets. *Nanoscale* **2014**, *6*, 12458–12462. [CrossRef] [PubMed]

40. Jariwala, B.; Voiry, D.; Jindal, A.; Chalke, B.A.; Bapat, R.; Thamizhavel, A.; Chhowalla, M.; Deshmukh, M.; Bhattacharya, A. Synthesis and characterization of ReS_2 and $ReSe_2$ layered chalcogenide single crystals. *Chem. Mater.* **2016**, *28*, 3352–3359. [CrossRef]

41. Hafeez, M.; Gan, L.; Li, H.; Ma, Y.; Zhai, T. Large-Area Bilayer ReS_2 Film/Multilayer ReS_2 Flakes Synthesized by Chemical Vapor Deposition for High Performance Photodetectors. *Adv. Funct. Mater.* **2016**, *26*, 4551–4560. [CrossRef]

42. Wei, J.; Bai, D.; Yang, L. Polymer photovoltaic cells with rhenium oxide as anode interlayer. *PLoS ONE* **2015**, *10*, e0133725. [CrossRef] [PubMed]

43. Addou, R.; McDonnell, S.; Barrera, D.; Guo, Z.; Azcatl, A.; Wang, J.; Zhu, H.; Hinkle, C.L.; Quevedo-Lopez, M.; Alshareef, H.N. Impurities and electronic property variations of natural MoS_2 crystal surfaces. *ACS Nano* **2015**, *9*, 9124–9133. [CrossRef]

44. Keyshar, K.; Gong, Y.; Ye, G.; Brunetto, G.; Zhou, W.; Cole, D.P.; Hackenberg, K.; He, Y.; Machado, L.; Kabbani, M. Chemical vapor deposition of monolayer rhenium disulfide (ReS_2). *Adv. Mater.* **2015**, *27*, 4640–4648. [CrossRef]

45. Rahman, M.; Davey, K.; Qiao, S.Z. Advent of 2D rhenium disulfide (ReS_2): Fundamentals to applications. *Adv. Funct. Mater.* **2017**, *27*, 1606129. [CrossRef]

46. Feng, Y.; Zhou, W.; Wang, Y.; Zhou, J.; Liu, E.; Fu, Y.; Ni, Z.; Wu, X.; Yuan, H.; Miao, F. Raman vibrational spectra of bulk to monolayer ReS_2 with lower symmetry. *Phys. Rev. B* **2015**, *92*, 054110. [CrossRef]

47. Miao, P.; Qin, J.K.; Shen, Y.; Su, H.; Dai, J.; Song, B.; Du, Y.; Sun, M.; Zhang, W.; Wang, H.L. Unraveling the Raman Enhancement Mechanism on 1T′-Phase ReS_2 Nanosheets. *Small* **2018**, *14*, 1704079. [CrossRef]

48. Lee, B.C.; Na, J.; Choi, J.H.; Ji, H.; Kim, G.T.; Joo, M.K. Probing Distinctive Electron Conduction in Multilayer Rhenium Disulfide. *Adv. Mater.* **2018**, *31*, 1805860. [CrossRef] [PubMed]

49. Wang, X.; Shinokita, K.; Lim, H.E.; Mohamed, N.B.; Miyauchi, Y.; Cuong, N.T.; Okada, S.; Matsuda, K. Direct and Indirect Exciton Dynamics in Few-Layered ReS_2 Revealed by Photoluminescence and Pump-Probe Spectroscopy. *Adv. Funct. Mater.* **2018**, *29*, 1806169. [CrossRef]

50. Pirkle, A.; McDonnell, S.; Lee, B.; Kim, J.; Colombo, L.; Wallace, R. The effect of graphite surface condition on the composition of Al_2O_3 by atomic layer deposition. *Appl. Phys. Lett.* **2010**, *97*, 082901. [CrossRef]

51. Liu, D.; Hong, J.; Wang, X.; Li, X.; Feng, Q.; Tan, C.; Zhai, T.; Ding, F.; Peng, H.; Xu, H. Diverse Atomically Sharp Interfaces and Linear Dichroism of 1T' ReS$_2$-ReSe$_2$ Lateral p-n Heterojunctions. *Adv. Funct. Mater.* **2018**, 1804696. [CrossRef]

52. Azcatl, A.; Qin, X.; Prakash, A.; Zhang, C.; Cheng, L.; Wang, Q.; Lu, N.; Kim, M.J.; Kim, J.; Cho, K. Covalent nitrogen doping and compressive strain in MoS$_2$ by remote N$_2$ plasma exposure. *Nano Lett.* **2016**, *16*, 5437–5443. [CrossRef] [PubMed]

53. Cho, S.; Kim, S.; Kim, J.H.; Zhao, J.; Seok, J.; Keum, D.H.; Baik, J.; Choe, D.-H.; Chang, K.J.; Suenaga, K. Phase patterning for ohmic homojunction contact in MoTe$_2$. *Science* **2015**, *349*, 625–628. [CrossRef]

54. Khosravi, A.; Addou, R.; Smyth, C.M.; Yue, R.; Cormier, C.R.; Kim, J.; Hinkle, C.L.; Wallace, R.M. Covalent nitrogen doping in molecular beam epitaxy-grown and bulk WSe$_2$. *APL Mater.* **2018**, *6*, 026603. [CrossRef]

55. Price, K.M.; Schauble, K.E.; McGuire, F.A.; Farmer, D.B.; Franklin, A.D. Uniform Growth of Sub-5-Nanometer High-κ Dielectrics on MoS$_2$ Using Plasma-Enhanced Atomic Layer Deposition. *ACS Appl. Mater. Interfaces* **2017**, *9*, 23072–23080. [CrossRef]

56. Hinkle, C.; Sonnet, A.; Vogel, E.; McDonnell, S.; Hughes, G.; Milojevic, M.; Lee, B.; Aguirre-Tostado, F.; Choi, K.; Kim, H. GaAs interfacial self-cleaning by atomic layer deposition. *Appl. Phys. Lett.* **2008**, *92*, 071901. [CrossRef]

57. Zhao, P.; Khosravi, A.; Azcatl, A.; Bolshakov, P.; Mirabelli, G.; Caruso, E.; Hinkle, C.L.; Hurley, P.K.; Wallace, R.M.; Young, C.D. Evaluation of border traps and interface traps in HfO$_2$/MoS$_2$ gate stacks by capacitance-voltage analysis. *2D Mater.* **2018**, *5*, 031002. [CrossRef]

58. Yang, J.; Kim, S.; Choi, W.; Park, S.H.; Jung, Y.; Cho, M.-H.; Kim, H. Improved growth behavior of atomic-layer-deposited high-k dielectrics on multilayer MoS$_2$ by oxygen plasma pretreatment. *ACS Appl. Mater. Interfaces* **2013**, *5*, 4739–4744. [CrossRef]

59. Zou, X.; Wang, J.; Chiu, C.H.; Wu, Y.; Xiao, X.; Jiang, C.; Wu, W.W.; Mai, L.; Chen, T.; Li, J. Interface Engineering for High-Performance Top-Gated MoS$_2$ Field-Effect Transistors. *Adv. Mater.* **2014**, *26*, 6255–6261. [CrossRef]

60. McDonnell, S.J.; Wallace, R.M. UV-Ozone Functionalization of 2D Materials. *JOM* **2018**, 1–14. [CrossRef]

61. Wallace, R.M. In-Situ Studies of Interfacial Bonding of High-κ Dielectrics for CMOS Beyond 22 nm. *Electrochem. Soc. Trans.* **2008**, *16*, 255.